PCCP

Correlating Structure and Transport Behavior in Li+ and O2 Containing Pyrrolidinium Ionic Liquids

Journal:	*Physical Chemistry Chemical Physics*
Manuscript ID	CP-ART-04-2019-002355.R1
Article Type:	Paper
Date Submitted by the Author:	20-Jun-2019
Complete List of Authors:	Gittleson, Forrest; Sandia National Laboratories; BMW Group Ward, Donald; Sandia National Laboratories, Jones, Reese; Sandia National Laboratories, Zarkesh, Ryan; Sandia National Laboratories California, Sheth, Tanvi; Sandia National Laboratories Foster, Michael; Sandia National Laboratories, Materials Chemistry

Journal Name

ARTICLE TYPE

Cite this: DOI: 00.0000/xxxxxxxxxx

Correlating Structure and Transport Behavior in Li^+ and O_2 Containing Pyrrolidinium Ionic Liquids †

Forrest S. Gittleson,[a,b] Donald K. Ward,[b] Reese E. Jones,[b*] Ryan A. Zarkesh,[b] Tanvi Sheth,[b] and Michael E. Foster[b]

Received Date
Accepted Date

DOI: 00.0000/xxxxxxxxxx

Ionic liquids are a unique class of materials with several potential applications in electrochemical energy storage. When used in electrolytes, these highly coordinating solvents can influence device performance through their high viscosities and strong solvation behaviors. In this work, we explore the effects of pyrrolidinium cation structure and Li^+ concentration on transport processes in ionic liquid electrolytes. We present correlated experimental measurements and molecular simulations of Li^+ mobility and O_2 diffusivity, and connect these results to dynamic molecular structural information and device performance. In the context of Li-O_2/Li-air battery chemistries, we find that Li^+ mobility is largely influenced by Li^+-anion coordination, but that both Li^+ and O_2 diffusion may be affected by variations of the pyrrolidinium cation and Li^+ concentration.

1 Introduction

Electrolyte dynamics have a profound influence on the kinetics, electrochemical stability, and transport processes that dictate lithium battery performance. The transport of electrolyte components significantly affects high power cell operation especially when one component, Li^+, for example, becomes locally depleted. Beyond-Li-ion chemistries that are reliant on soluble species for their functionality, such as Li-air and Li-S, are affected by similar issues. The Li-air/Li-O_2 system, in particular, suffers from poor oxygen solubility and diffusivity in liquid electrolytes which impacts the maximum operating current and energy density[1]. Such fundamental transport phenomena are deserving of more attention as we seek to discover and design new electrolytes.

Several families of electrolyte solvents have been evaluated for the challenging Li-air system and none have been deemed adequate for practical application. Dimethyl sulfoxide (DMSO) offers good rate capability, but is unstable against Li metal anodes and superoxide products[2–4]. Glyme solvents are more stable against superoxides, but are either too volatile or too viscous, depending on their molecular chain length[5,6] and are teratogenic. Ionic liquids (ILs) are more stable against Li metal and superoxides and offer better reversibility than many non-aqueous solvents[7,8]; yet they generally suffer from high viscosities that result in poor rate capability[9,10].

The subset of pyrrolidinium-based ionic liquids are class-leading in stability,[11] but there is little understanding of how systematically varying the ionic liquid structure can influence electrolyte dynamics.

A few reports have investigated the effect of ionic liquid structure on electrolyte properties. Le *et al.*[12] showed that increasing the alkyl ligand length on the cation of an alkylammonium IL reduces its ionic conductivity, as does increasing the concentration of Li^+. The formation of less-mobile ionic clusters around Li^+ ions and an increase in viscosity are dual contributors to this phenomena. A similar influence of IL cation ligand length on self-diffusion and conductivity is also reflected in pyrrolidinium and imidazolium-based IL electrolytes[13,14]. An exchange of alkoxy ligands on these same cations, has shown some beneficial properties such as lower viscosity and higher conductivity as well as the potential to coordinate metal ions through electronegative oxygens[15–18]. To better understand the dynamics of these systems, a number of computational investigations have been conducted which focus on ion interactions. Several of these show that the interaction between Li^+ and the anion is so strong as to influence the mechanism of Li^+ movement in the liquid[19–22]. These studies find that Li^+ is more likely to move by "structure" diffusion, *i.e.* hopping between low energy anion-coordinated sites or exchanging anions around a central Li^+, than "vehicular" diffusion, where the Li^+ solvation shell remains intact and the motion is more classically Brownian[19,20]. As such, the diffusion coefficient of Li^+ is expected to be significantly lower than that of the anion or the IL cation since many of these species are free and not encumbered by solvation. Though Li^+-anion coordination is the key interaction, some experimental work has suggested that pyrrolidinium

[a] *BMW Technology Office USA, 2606 Bayshore Parkway, Mountain View, CA 94043, USA*
[b] *Sandia National Laboratories, P.O. Box 969, Livermore, CA 94551, USA*
* *rjones@sandia.gov*

cations also coordinate with Li^+ over long ranges (in the second coordination sphere) and so the structure of the cation may still influence Li^+ mobility[20].

By systematically varying the IL structure, we can better understand the impact of chemistry on the mobility of electrolyte components. In general, the relationship between mobility of the limiting reactant and cell power can be summarized (for an idealized flat electrode) by the rate limiting current[23]:

$$i_{\text{limiting}} = nF\frac{Dc}{\delta_0}\ , \tag{1}$$

where n is the number of electrons in the rate limiting reaction, F is Faraday's constant relating species concentration to charge density, D is the reactant diffusion coefficient, c is the reactant concentration, and δ_0 is the characteristic thickness of the stagnant electrolyte layer across which the reactant must diffuse. The stagnant layer near the electrode scales with the viscosity of electrolyte and may be on the order of tens of nanometers in viscous fluids; hence, an increase in viscosity with all other factors being equal leads to a decrease in i_{limiting}. Similarly, in Eq. (1), the current density is directly proportional to the concentration and the diffusivity of the limiting reactant; thus, increases in these factors should lead to increases in i_{limiting}, assuming no significant cross-effects. While these scaling relationships are not sufficiently accurate for direct application in battery cell design, they can provide guiding principles for electrolyte selection.

In Li-ion batteries, the rate limiting component is Li^+ (if the cell is not otherwise kinetically limited by the intercalation reaction at the electrode). In Li-air cells, however, either Li^+ or soluble O_2 may be rate limiting to the series of reactions that yield Li_2O_2 or LiO_2 products. For common cell configurations, O_2 is normally limiting due to its low solubility in many non-aqueous electrolytes[1,24,25], but ionic liquid electrolytes present a system where either component may be limiting due to high electrolyte viscosity and low ionic mobility. To select an appropriate electrolyte, we must understand which conditions and chemistries dictate these modes of cell operation.

In this work, we focus on reactant transport and related electrolyte properties. We investigate several pyrrolidinium-based ionic liquids with a bis(trifluoromethanesulfonyl)imide (TFSI) anion over a range of Li^+ concentrations and IL cation structures to understand the impacts on solvation behavior, ion mobility, and reactant diffusion. After describing the electrolyte synthesis, experimental measurement, molecular model, and property measurement methods, we report the experimental and simulation results. We focus on properties that directly affect the limiting discharge rate of Li-air/Li-O_2 cells. In the final sections, we connect experimental measurements of transport properties and device performance with molecular simulation of solvation and transport behavior to elucidate the impact of ionic liquid structure and lithium content on cell performance.

2 Methods

We used a combination of experimental and simulation methods to investigate the properties of pyrrolidinium (Pyr) ILs as electrolytes. As can be seen in Fig. 1, the Pyr molecules we studied are composed of a carbon and nitrogen-containing ring where the single nitrogen is bonded to a methyl carbon and an alkyl ligand of variable length. The four particular Pyr cations are, by abbreviation: $Pyr1.3^+$, $Pyr1.2O1^+$, $Pyr1.4^+$, $Pyr1.6^+$, in order of ligand length. $Pyr1.2O1^+$ is approximately the same size and configuration as $Pyr1.4^+$ but with different charge distribution and chain flexibility due to the substitution of an oxygen for one of the carbons in the alkyl ligand. In solution the Pyr cations are charge balanced by $TFSI^-$ anions. We examined these ILs with various LiTFSI salt concentrations (0.0M, 0.1M, 0.5M and 1.0M) to explore molarity effects. For comparison with a common, non-ionic solvent, we also evaluated dimethyl sulfoxide (DMSO) with LiTFSI.

2.1 Experiment

Electrolytes consisted of anhydrous dimethyl sulfoxide (DMSO, Sigma Aldrich), N-methyl-N-propyl pyrrolidinium bis(trifluoromethanesulfonyl)imide (Pyr1.3-TFSI), N-methyl-N-butyl pyrrolidinium bis(trifluoromethanesulfonyl)imide (Pyr1.4-TFSI), N-methyl-N-hexyl pyrrolidinium bis(trifluoromethanesulfonyl)imide (Pyr1.6-TFSI), or N-methyl-N-methoxyethyl pyrrolidinium bis(trifluoromethanesulfonyl)imide (Pyr1.2O1-TFSI) with various concentrations of lithium bis(trifluoromethanesulfonyl)imide (LiTFSI, 99.95% trace metals basis Sigma Aldrich). All solvents were treated with molecular sieves for at least 3 days to remove residual water.

The IL precursors: 1-bromopropane, 1-bromobutane, 2-bromoethyl methyl ether, and 1-bromohexane, were purchased from Sigma Aldrich and stored with activated molecular sieves in a sealed container. N-methyl pyrrolidine was purchased from Sigma Aldrich, sparged with N_2, stored over activated molecular sieves, and then distilled under vacuum before use.

Ionic liquids were synthesized from commercially available precursors with methods similar to those previously reported[26]. Four methyl-X pyrrolidinium bis(trifluoromethanesulfonyl)imide ionic liquids with varying (X) ligands (*i.e.* Pyr1.X) were prepared and purified. Nucleophilic substitution utilizing N-methyl pyrrolidine was carried out at elevated temperatures in toluene resulting in precipitation of the bromide salt. First, N-methyl pyrrolidine was dissolved in dry, air free, toluene and treated with the alkyl bromide. The reaction mixture was heated to 50 °C under an atmosphere of N_2 to exclude water from the reaction. After 12 hr, the pyrrolidinium bromide salt had precipitated from the reaction mixture and was isolated by filtering over a medium porosity glass frit in air.

The resulting bromide salt was conveyed to the next step by dissolving the pyrrolidinium bromide salt in deionized (DI) water followed by treatment with activated carbon. The resulting black slurry was heated to 55 °C and held at this temperature for 3 days to remove trace impurities. The activated carbon was filtered away from the clear solution using a fine porosity glass frit in air. Next, the clear filtrate was treated with lithium bis(trifluoromethanesulfonyl)imide (LiTFSI) dissolved in deionized water. The resulting ionic liquids were sufficiently hydropho-

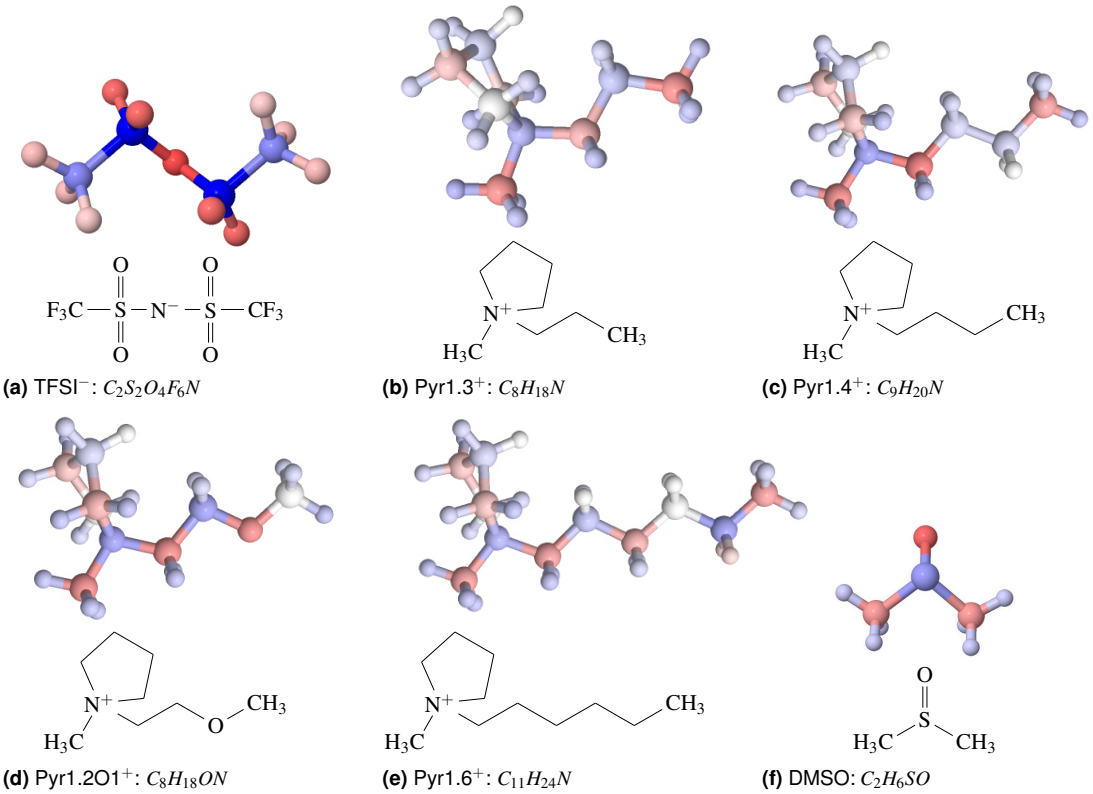

Fig. 1 Molecular structures. Atoms colored by partial charge (red:-1, blue:+1).

bic to separate from the water; hence, the clear viscous liquids were isolated by decanting away the water and washing 3 times with fresh deionized water. The Pyr1.X-TFSI salts were then treated with more activated carbon and filtered to remove any trace impurities. The removal of impurities was monitored using UV-visible spectroscopy. The resulting ILs were dried further under vacuum and stored over molecular sieves. Nuclear magnetic resonance spectroscopy (NMR) was used to confirm the structure and purity of the ILs, consistent with previous reports[16,27]. Yields of the Pyr1.3-TFSI, Pyr1.4-TFSI, Pyr1.6-TFSI and Pyr1.2O1-TFSI were ≈90% after the two step synthesis and purification procedures.

Physical properties of the various electrolytes were measured experimentally. Absolute viscosities ν were measured using a RheoSense m-VROC. Densities ρ were determined from volume and mass measurements. The diffusion coefficient D and concentration of oxygen c in various ionic liquids were obtained using microelectrode chronoamperometry, where a potential was applied to the electrode and the resulting current was measured. Gold microelectrodes (CH Instruments) with ≈16 μm measured diameter (12.5 μm nominal diameter) were used as the working electrode, a Pt wire as the counter electrode and an Ag wire as the pseudoreference electrode. All electrodes were polished, rinsed and dried prior to use. Approximately 2-3 mL of ionic liquid were used for each chronoamperometry experiment and up to 5 replicates were performed on each sample. The surface area of microelectrodes was measured independently after each replicate (following washing with acetone and water) using a solution of 1 mM ferrocenemethanol with 0.1 M $NaNO_3$ in DI water as supporting electrolyte. Chronoamperometry of this solution at 0.4 V *vs.* Ag was used to derive the electrode radius R from fitting the current i as a function of time t to the Shoup-Szabo equation:[28,29]

$$i(R,t) = 4RDFc\,f\left(\sqrt{\frac{R^2}{4Dt}}\right), \qquad (2)$$

with the dimensionless function $f(x) = 0.7854 + 0.8862x + 0.214\exp(-0.7823x)$, using an accepted value of the diffusion coefficient $D = 7.8 \times 10^{-6}$ cm^2/s of ferrocenemethanol.[30] By simultaneously fitting the data to Eq. (2) and the Cottrell equation:

$$i(t) = Fc\sqrt{\frac{D}{\pi t}}, \qquad (3)$$

the diffusion coefficient D of ferrocenemethanol was found to be $\approx 4.3 \times 10^{-6}$ cm^2/s, slightly lower than reported values, perhaps due to the unique microelectrode geometry. To determine the diffusion coefficient D and concentration c of dissolved oxygen in the Pyr ILs, chronoamperometry was performed in a glovebox purged with ≈1 atm dry air at -1.6 V *vs.* Ag, consistent with mass transport-limited oxygen reduction, determined by linear sweep voltammetry. This chronoamperometric data was simultaneously fitted to the Cottrell equation Eq. (3) for time $t \in [0.05, 1.00]$ s and the Shoup-Szabo equation, Eq. (2), for time $t \in [0.05, 20]$ s using OriginLab software given the electrode radius, R, from the fer-

rocenemethanol data and n=1, which is consistent with the reaction[23] $O_2 + e^- \leftrightarrow O_2^-$.

The conductivity of each electrolyte was determined using impedance analysis of symmetric Li-Li coin cells. After impregnation of a glass fiber separator with electrolyte, sealing, and equilibration of cells for a minimum of 48 hrs, impedance was measured and electrolyte conductivities were calculated.

Full Li-O_2 coin cells were assembled by stacking a 15.6 mm diameter Li metal anode (on top of a wave spring and shim), a 17 mm Whatman GF/A glass fiber separator (impregnated with 60 μL electrolyte) and a 15 mm diameter, 235 μm thick Sigracet 25BC carbon electrode with the microporous layer oriented toward the separator. A flattened Ni foam (MTI Corp.) spacer was placed between the oxygen electrode and coin cell case to increase the air headspace and improve conductivity across the carbon electrode. Lithium metal counter electrodes, stainless steel CR2032 coin cell cases with perforated tops, wave springs, and stainless steel shims were sourced from MTI Corp. The effective, electrochemical surface area (ECSA) of the oxygen electrode was 83 cm^2, determined by measurement of the double layer capacitance using a symmetric cell with a 1M LiTFSI/Pyr1.4-TFSI electrolyte[1]. This area is significantly larger than the apparent area given by the outer dimensions of the electrode due to its porosity. After crimping, cells were allowed to equilibrate in a dry air glovebox ($\leq$ 1 ppm H_2O) at open circuit potential for 6 hrs before cycling. Cells were discharged at room temperature in $\approx$1 atm dry air using a BioLogic MPG-2 battery tester by drawing current galvanostatically at various rates from open circuit voltage to 2.0 V.

2.2 Simulation

For the simulations, we constructed molecular models of the LiTFSI/Pyr1.X-TFSI and LiTFSI/DMSO electrolytes using the AMBER[31–33] unified empirical potential composed of short-range van der Waals, long-range Coulombic and covalent intramolecular interactions:

$$\Phi = \underbrace{\sum_{\alpha<\beta} 4\varepsilon_{ab}\left(\left(\frac{\sigma_{ab}}{r_{\alpha\beta}}\right)^{12} - \left(\frac{\sigma_{ab}}{r_{\alpha\beta}}\right)^{6}\right)}_{\text{van der Waals}} + \underbrace{\frac{1}{4\pi\varepsilon}\sum_{\alpha<\beta}\frac{q_\alpha q_\beta}{r_{\alpha\beta}}}_{\text{Coulomb}} \quad (4)$$

$$+\sum_I\Big[\sum_{\alpha,\beta\in M_I} k_{ab} r_{\alpha\beta}^2 + \sum_{\alpha,\beta,\gamma\in M_I} k_{abc}\theta_{\alpha\beta\gamma}^2$$

$$\underbrace{+\sum_{\alpha,\beta,\gamma,\mu\in M_I} k_{abcd}(1+\cos(n_{abcd}\phi_{\alpha\beta\gamma\mu} - \phi_{abcd}))\Big]}_{\text{covalent}}$$

The interaction energy Φ is dependent on the atomic positions $\mathbf{x}_\alpha$, through pairwise distances $r_{\alpha\beta}$, 3 atom angles $\theta_{\alpha\beta\gamma}$, and 4 atom dihedral angles $\phi_{\alpha\beta\gamma\mu}$, and point charges q_α. The van der Waals interactions are represented with a Lennard-Jones (LJ) model. The Coulomb interactions take the usual form; however, a particle-particle particle-mesh (PPPM) solver[34] was employed to compute the long-range Coulomb interactions beyond a 16 Å cutoff and direct summations were used for the remainder. The covalent intramolecular interactions were modelled with harmonic potentials for pair bond distances $r_{\alpha\beta}$ and for 3 atom angles $\theta_{\alpha\beta\gamma}$, and a trigonometric potential for 4 atom dihedral angles $\phi_{\alpha\beta\gamma\mu}$ (torsions). The per-species LJ parameters σ_{ab} and ε_{ab}, as well as the parameters for the intramolecular forces, were, in general, tuned to the structural and vibrational properties of individual molecules. All parameters except the point charges q_α were taken from literature[14,33,35–39]. The point charges were obtained from *ab initio* calculations performed with Gaussian[40] on the optimized geometry of the isolated molecules using Møller-Plesset theory (MP2) with the def2TZVP basis set. The partial atomic charges shown in Fig. 1 were extracted with the CHelpG scheme[41] using the electron density obtained from the second order MP2 theory. All the molecular dynamics simulations were performed with LAMMPS[42].

With this potential, we constructed each system with 2048 solvent molecules (DMSO or Pyr1.X), 2 O_2 molecules and the number of Li^+ ions, N_{Li}= { 0, 60, 300, 600}, corresponding to {0.0, 0.1, 0.5, 1.0}M Li^+ concentrations. Charge balance gives the required number of $TFSI^-$, for DMSO: $N_{\text{TFSI}} = N_{\text{Li}}$ and for Pyr1.X-TFSI: $N_{\text{TFSI}} = N_{\text{Li}} + N_{\text{Pyr}}$. Initially, the Pyr1.X-TFSI or DMSO solvent molecules were randomly oriented on a large unit cell, face centered cubic lattice while the O_2, Li^+ and anions were randomly positioned in the simulation domain. After construction, all systems were initialized with a series of relaxation steps. First each system was relaxed with constant volume dynamics with a limited maximum atomic displacement of 0.01 Å per 1 fs timestep. This stage ensures that initial high-energy interactions were stably relaxed in order to proceed with standard molecular dynamics (MD) at reasonable time steps. Then a pressure-controlled heating cycle was applied to each system. In this stage, velocities were re-initialized with a Gaussian distribution at 600K and then 100 ps of isothermal, isobaric dynamics was run at this temperature and 1 atm with a Nosé-Hoover thermo-barostat. Following this stage, the pressure was increased to 10 GPa while decreasing the temperature to 300 K for 100 ps, and then the pressure was decreased to 1 atm over 100 ps. These steps allow for unlikely local configurations to transition to more representative ones. Once each system reaches 300 K and 1 atm, it was equilibrated for 200 ps at constant temperature and pressure while the energy and volume were monitored to ensure convergence and equilibration.

We used a variety of methods to estimate both the structural and transport material properties of the electrolytes[43]. The density was calculated using an average volume from standard isothermal, isobaric dynamics. The melt temperature was determined by the knee in the density versus temperature curve for slow temperature cycles (since phase coexistence methods are impractical with these systems). Specifically, cycling between 200K and 600K over 0.3 ns multiple times allowed us to identify the regimes separating the solid-liquid transition based on distinct trends in thermal expansion. The estimated melt temperature was found by intersection of the two volume-temperature trends, further details can be found in Ward *et al.*[44]. The calculated melt temperature T_m^* for a particular solvent allows us to define a homologous temperature $T^* = \frac{T_m^*}{T_m} T$ based on the target temperature (T=300 K) and the actual melt temperature based

on reported literature, T_m. This rescaling was necessary since the model melt temperatures for the Pyr1.X-TFSI systems where significantly larger than the actual ones, hence at 300 K our model electrolytes behaved like solids with some mobile components (*i.e.* the estimated viscosities were high, anisotropic, and did not converge well). Since the estimated T_m^* was relatively insensitive to Li^+ salt content and the errors in the T_m^* estimates were comparable to the differences across electolytes, we assumed a uniform scaling across all the systems and collected Pyr1.X-TFSI transport properties at $T^* = 385$ K. Given the often-used Arrhenius relation for viscosity and other properties governed by molecular kinetics, we expect an exponential dependence on temperature. Other side-effects of this modeling decision will be discussed in Sec. 3.2.2 and Sec. 4.2.

The Li^+ solvation was characterized with per-species coordination derived from the radial distributions. The coordination of species a with b, C_{ab}, was calculated with :

$$\mathrm{C}_{ab}(R) = \frac{1}{N_b}\left\langle \sum_{\alpha\in\mathscr{G}_a}\sum_{\beta\in\mathscr{G}_b} \iota(\|\mathbf{x}_\alpha - \mathbf{x}_\beta\| < R)\right\rangle , \tag{5}$$

and quantifies the average number of species a within a sphere of radius R centered on an atom of type b. Here $\mathscr{G}_a$ is the group of all atoms of type a, $\mathbf{x}_\alpha$ is the position of atom α, ι is the indicator function whose value is 1 if its argument is true and 0 if its false, and $\langle\bullet\rangle$ is an equilibrium time average. We calculate the persistence, P_{ab}, of particular molecular constituent atoms of species a in the solvation shells of species b via:

$$\mathrm{P}_{ab}(R,\tau) = \frac{1}{N_b}\left\langle \sum_{\alpha\in\mathscr{G}_a}\sum_{\beta\in\mathscr{G}_b} \iota(\tau_{\alpha\beta}(R) < \tau)\right\rangle \tag{6}$$

where

$$\tau_{\alpha\beta}(R) = \Delta t \sum_{i=0}^{N} \iota(r_{\alpha\beta}(t_i) < R) . \tag{7}$$

This metric counts the number of times any atom of species a appears in a shell of radius R around an atom of species b and indicates how long a solvating species stays in the shell of another species. The persistence is related to the coordination by $P_{ab}(R,0) = C_{ab}$ and is an increasing function of the radius R and a decreasing function of the residence time τ. It will give us insights into the degree of hopping ("structural") versus intact solvation ("vehicular") diffusion.

For viscosity, we use a well-known Green-Kubo relation:

$$\begin{aligned}\nu &= \frac{1}{3k_BT}\int_0^\infty \langle \varsigma(0)\cdot\varsigma(t)\rangle \,\mathrm{d}t \qquad (8)\\ &\approx \frac{1}{3k_BT}\left(\frac{1}{2N}\sum_{i=0}^{N}\varsigma(t_i)\cdot\varsigma(t_i) + \sum_{j=1}^{N}\frac{1}{N-j}\sum_{i=1}^{N-j}\varsigma(t_i)\cdot\varsigma(t_i+j\Delta t)\right)\Delta t\end{aligned}$$

with $\varsigma = (\sigma_{23},\sigma_{13},\sigma_{12})$ being the vector of shear stress components derived from a virial expression and N being the number of time samples.

For the O_2 diffusion coefficient we use the usual Einstein relation for tracer diffusion:

$$D = \frac{1}{3}\int_0^\infty \langle \mathbf{v}_\alpha(0)\cdot\mathbf{v}_\alpha(t)\rangle \,\mathrm{d}t = \frac{1}{6}\lim_{t\to\infty}\frac{\partial\left\langle\|\mathbf{x}_\alpha(t)-\mathbf{x}_\alpha(0)\|^2\right\rangle}{\partial t} , \tag{9}$$

where $\mathbf{v}_\alpha$ is the velocity of atom α and we approximate

$$\left\langle\|\mathbf{x}(t_i)-\mathbf{x}(0)\|^2\right\rangle \approx \frac{1}{N-i}\sum_{j=0}^{N-i}\|\mathbf{x}(t_{j+i})-\mathbf{x}(t_j)\|^2 . \tag{10}$$

For the ionic conductivity, $\sigma = \sum_a \sigma_a$, we use Ciccotti and Jacucci's method[45] for each species partial conductivity σ_a, where we measure the current $\mathbf{i} = \sum_a \mathbf{i}_a$ induced by an external field E in the limit of the external field to zero:

$$\sigma_a = \lim_{E\to 0}\frac{\|\mathbf{i}_a(E)\|}{E} \approx e z_a c_a \frac{\|\mathbf{v}_a(\delta E)\|}{\delta E} . \tag{11}$$

Here the species current density is $\mathbf{i}_a = e z_a n_a \mathbf{v}_a$, e is the unit of charge, z_a is the valence of species a, $c_a \equiv \frac{N_a}{V}$ is molar species concentration, N_a is the number of species a in the system, V is the system volume, and the average species velocity $\mathbf{v}_a$ for species a is

$$\mathbf{v}_a \equiv \frac{1}{N_a}\left\langle\sum_{\alpha\in\mathscr{G}_a}\mathbf{v}_\alpha\right\rangle . \tag{12}$$

The small perturbation δE is chosen to be sufficiently large to overcome thermal noise in $\mathbf{v}_a$. (The issue of signal-to-noise in measuring $\mathbf{i}_a$ in the $E\to 0$ limit will be discussed in the following section.) The per-species conductivity $\sigma_a = e z_a c_a \mu_a$ is related to the mobility μ_a of species a. Since the external field E adds kinetic energy to the system, a thermostat is necessary. We use a Nosé-Hoover thermostat that preserves momentum and is temperature corrected for the average/streaming velocity $\mathbf{v}_a$ of each species a:

$$T = \frac{1}{3k_B}\sum_a \frac{1}{N_a}\sum_{\alpha\in\mathscr{G}_a} m_\alpha\|\mathbf{v}_\alpha - \mathbf{v}_a\|^2 . \tag{13}$$

For all the transport property simulations including the diffusivity and mobility calculations, we allowed 20 ns to accommodate any transients, and then used 500 ns of thermostatted dynamics for collecting the average flux, coordination, and related information.

3 Results

We measured various electrolyte properties to give indications of cell performance, and built simulations to estimate corroborating properties and to provide insights into structure and transport. Generally speaking, we explored the effects of structure and salt concentration on the transport properties particularly relevant to IL electrolytes in a Li-air cell: ionic conductivity and oxygen diffusivity. We also measured and calculated properties, including viscosity and density, to provide a strong connection between experiment and theory.

3.1 Experiments

The physical properties of selected IL electrolytes were measured and are reported in Table 1. Both density and viscosity were observed to increase with higher LiTFSI concentrations across all

systems. The magnitude of the increase in viscosity from 0.0 M to 1.0 M LiTFSI suggests significant changes to the ion-ion coordination environment when adding Li^+ salts. We note that the bulk conductivity of IL electrolytes generally decreases with increasing Li^+ salt concentration, as seen in Fig. 2, consistent with previous work[22,46,47]. While we were not able to deconvolve the conductivities of particular electrolyte ion species from our experiment, these previous reports have shown that increasing Li^+ concentration leads to a decline or stagnation in Li^+ partial conductivity and a decline in Li^+ free diffusion. This implies that our observed decrease in bulk conductivity is likely also reflected in the mobility of Li^+ ions. It is plausible that LiTFSI coordination has a significant influence on Li^+ mobility and that varying the structure of the Pyr cation largely affects mobility through the solution viscosity. Thus, it is important to distinguish between ionic conductivity that is limited by "vehicular" diffusion (influenced by viscosity) or by "structure" (influenced by diffusion by the exchange of anions in a solvation sphere or cation hopping).

In the context of Li-air batteries, we also studied the transport of O_2 molecules in the electrolyte using microelectrode techniques. Because LiO_2 and Li_2O_2 products of O_2 reduction are known to precipitate rapidly in Li^+-containing ionic liquids[48], we only measured O_2 transport in pristine ILs without Li^+. Using chronoamperometric techniques and Shoup-Szabo analysis[28], the concentration of O_2 in solution in equilibrium with ≈1 atm dry air, c^*, and the O_2 diffusion coefficient, D, were derived. We find that for Pyr ILs with an alkyl ligand, oxygen solubility decreases with increasing ligand length (see Table 1). Meanwhile, oxygen diffusivity increases across the same sequence: $Pyr1.3^+$, $Pyr1.4^+$, $Pyr1.6^+$. These findings imply that longer alkyl chains provide molecular environments which facilitate O_2 diffusion. Previous reports have linked the formation of interconnected apolar domains by alkyl groups in ILs to the improved diffusion of solutes, like O_2, with limited ion-solute interaction[49–51]. In particular, the nonpolar nature of O_2[49] and the tendency of the ILs to form nanoscale, molecular structures[50,51] can be determining factors. At the same time, long alkyl ligands with multiple axes of rotation are likely to fill the unoccupied volume in the liquid, reducing the spaces in which O_2 can reside, thus decreasing solubility. The relationship between "free volume" and oxygen concentration was previously reported by Neale *et al.*[29] with a similar reasoning, but this theory is incomplete, as it fails to account for differences in electrostatics with different molecular structures[1,52]. Since we are unable to reliably measure the solubility or diffusivity of O_2 in Li^+-containing ILs, the influence of additional salt species must be studied by means such as simulation. It is, however, reasonable to expect some influence on these parameters through changes in free volume, electrostatics and viscosity with increased LiTFSI concentration.

The discharge capacity of the Li-air cells versus the discharge rate is shown in Fig. 3a and elucidates rate limiting behavior as a function of Pyr cation structure. The rate limiting current is a cell-specific property tied to the diffusivity and the concentration of the rate limiting reactant, in this case O_2 or Li^+. We previously used a survey of discharge capacity versus discharge rate to identify differences in the rate limiting behavior of Li-air electrolytes with aprotic solvents[1], concluding that O_2 supply is limiting in most cases. Other studies have shown a connection between discharge capacity and discharge rate in tetraglyme electrolytes[53,54], but attributed this exclusively to differences in product growth on the electrode while neglecting the impact of reactant transport. As we focus on the rate limiting current with IL electrolytes, it is appropriate to assess behavior with respect to transport. The results presented in Fig. 3a show that for cells with Pyr1.3-TFSI, Pyr1.4-TFSI and Pyr1.6-TFSI with 1.0M LiTFSI the rate limiting current (signified by a step change in capacity) appears to be ≈0.001 mA/mm^2 in terms of the measured ECSA. The rate behaviors and discharge capacities are similar across these three electrolytes, indicating that there is no fundamental difference in the limiting mechanism. Regardless of if we assume that O_2 or Li^+ is the limiting reactant in these high concentration Li^+ electrolytes, we note that differences in Pyr ligand length have a minimal effect on transport. In our previous work[1], we demonstrated that 1.0M LiTFSI/DMSO and 1.0M LiTFSI/TEGDME electrolytes in cells with the same architecture, exhibit rate limiting currents of ≈2 mA/mm^2 ECSA and ≈0.08 mA/mm^2 ECSA, roughly 2–3 orders of magnitude higher than any 1.0M LiTFSI/Pyr1.X-TFSI electrolytes. These traditional aprotic solvent electrolytes yield cells that also exhibit 2–6 times higher capacities, depending on discharge rate.

In Fig. 3a, the 1.0M LiTFSI/Pyr1.2O1-TFSI electrolyte exhibits no step change in capacity at ≈0.001 mA/mm^2 ECSA, as with other IL electrolytes. Instead, it shows a gradual increase in discharge capacity with a decrease in discharge rate. Thus, the rate limitation for this electrolyte likely lies at higher currents than for IL electrolytes with purely alkyl ligands. A change in the oxygen reduction mechanism, or Li^+ solvation, due to the ether group in the $Pyr1.2O1^+$ cation are the likely culprits, particularly as the other IL electrolytes listed in Table 1 exhibit similar physical properties.

Fig. 3b illustrates the impact of LiTFSI concentration on the capacity-rate relationship. For Pyr1.4-TFSI electrolytes, we note that the 0.5M LiTFSI electrolyte yields what appears to be the highest limiting current. This surprising finding suggests that the rate limiting current is optimized by balancing the normally limited O_2 supply and the Li^+ supply to the reaction sites of the electrodes. As in aprotic solvent electrolytes[1], Li^+ supply is rate limiting at low Li^+ concentrations and yet negatively impacts O_2 supply at higher Li^+ concentrations. Thus, an optimal intermediate concentration exists at which the full cascade of oxygen reduction reactions proceeds efficiently. The differences in discharge capacity at low rates between the three electrolytes can be attributed to different passivation behaviors of the oxygen reduction products. It is worth noting that the LiTFSI concentration dependence is not unique to Pyr1.4-TFSI. We repeated this study for Pyr1.6-TFSI electrolytes across LiTFSI concentrations and found the same trend (not shown), where the 0.5M LiTFSI concentration also produces the highest limiting current.

	LiTFSI [M]	ρ [g/mL]	T_m [K]	ν [cP]	c^* [mM]	D [μm^2/ms]	σ [S/m]
DMSO	0.0	1.100	–	2.07	0.330	–	–
	0.1	1.121		2.29		1.28	0.156
	0.5	1.163		2.80		1.40	0.432
	1.0	1.217		3.97		1.09	0.740
Pyr1.2O1-TFSI	0.0	1.570	233	60.48	10.16	0.0542	0.122
	0.1	1.670		66.24			0.0927
	0.5	1.640		122.70			0.0589
	1.0	1.840		231.18			0.0515
Pyr1.3-TFSI	0.0	1.441	284	72.27	2.17	0.190	0.100
	0.1	1.449		80.06			0.123
	0.5	1.476		145.69			0.0887
	1.0	1.507		305.87			0.0408
Pyr1.4-TFSI	0.0	1.400	267	92.60	1.60	0.269	0.0906
	0.1	1.412		102.77			0.0290
	0.5	1.441		189.15			0.0279
	1.0	1.460		454.50			0.0349
Pyr1.6-TFSI	0.0	1.347	275	135.02	1.38	0.329	0.0388
	0.1	1.360		144.80			0.0225
	0.5	1.390		269.06			0.0222
	1.0	1.424		568.71			0.0168

Table 1 Measured properties: mass density ρ, O_2 self diffusion coefficient D, viscosity ν, ionic conductivity σ, at 300 K. Oxygen solubility c^* for 0.0M LiTFSI/DMSO at 298.2 K, 0.206 bar O_2 is from Battino[55]. Melt temperature T_m is from Appetecchi *et al.*[9].

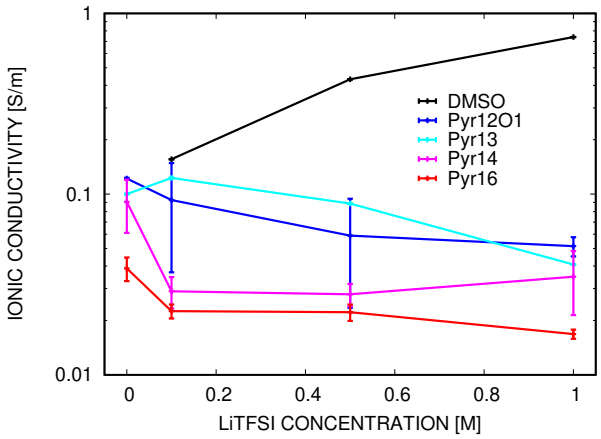

Fig. 2 Experimental measurement of total ionic conductivity for various IL electrolyte compositions.

3.2 Simulation

The simulations described in this section give us additional insight into liquid phase molecular interactions and how these affect cell performance. With the molecular model described in Sec. 2.2, we simulated the molecular dynamics of the ILs and extracted structural information and transport properties. In particular, we examined how Li^+ is solvated, both in terms of the traditional average coordination (through the radial distribution function (RDF)) and also the transient aspects: the persistence of solvation shells and the degree to which ions co-transport in a flow induced by electrical bias. In addition, we estimate the relevant transport coefficients, including per-species partial ionic conductivities. Since some of the methods are new and the molecular model has not been widely used to represent ILs, we use a LiTFSI/DMSO electrolyte for validation and comparison. Lastly, since the Pyr IL solvents are marginally above their melt temperatures and have a tendency to become glassy, we simulated most of the Pyr properties at a higher, homologous temperature which has some side-effects that will be discussed.

3.2.1 LiTFSI/DMSO

We examined the LiTFSI/DMSO system with the same interatomic potential as the ILs to provide a baseline for the accuracy of the AMBER potential, and as a non-ionic solvent system to compare to the IL results. With regard to the determining the ionic conductivity over a range of external electric fields, E=0–0.1V/Å, Fig. 4 shows that the mean (streaming) velocity of each component of the electrolyte is small compared to the average thermal velocity (the width of the Maxwell-Boltzmann distribution). The E field at these levels is also too weak to dissociate solvation structures. * Also it is notable that the velocity distributions in Fig. 4(inset) re-

* Assuming the main effects are the Coulomb forces between oppositely charged species, the E field at which an ion and another species in its solvation shell dissociate is $E_{\max}(r) \approx \frac{1}{(4\pi\epsilon_0)} \frac{q}{r^2}$, where q is the charge of the solvating species which we will take to be 1 e, given the ions in solution. Specifically, $E_{\max}$ (3Å) = 1.6 V/Å for a molecule nominally in the first shell of Li^+ in this electrolyte and $E_{\max}$ (8Å) = 0.2 V/Å for a molecule nominally in the second shell. (The first and second shells are defined by the plateaus in the coordination in Fig. 5a and are similar in magnitude to those in Fig. 7.) On the other hand, there is a minimum E that allows us to observe significant ionic flux over MD timescales. Roughly speaking, $v_{\min} \approx 100$ Å/100×10^3 ps = 0.001 Å/ps, based on the order of magnitude of our system size and feasible simulation time. Now, using the order of magnitude of the expected conductivity $\sigma \approx 0.1$ S/m (which corresponds to $\mu \approx 0.1$ Å^2/ps-V at 1M), we obtain $E_{\min} = v_{\min}/\mu \approx 0.01$ V/Å. Since this approximate analysis of the perturbation is generic, we will use this range of E in the following study of Pyr-based electrolytes.

	LiTFSI [M]	ρ [g/mL]	T_m [K]	ν [cP]	D [μm^2/ms]	σ [S/m]	σ_{Li} [S/m]	σ_{TFSI} [S/m]	σ_{Pyr} [S/m]
DMSO	0.0	1.11	–	2.4	1.26	–	–	–	–
	1.0	1.26	–	6.5	0.79	0.61	0.29	0.32	–
Pyr1.2O1-TFSI	0.0	1.57/1.51	354	46.1	0.34	–	–	–	–
	1.0	1.62/1.58	354	37.0	0.17	0.050	-0.024	0.025	0.049
Pyr1.3-TFSI	0.0	1.53/1.47	362	26.4	0.48	–	–	–	–
	1.0	1.58/1.54	361	43.6	0.29	0.021	-0.042	0.020	0.043
Pyr1.4-TFSI	0.0	1.49/1.42	365	23.6	0.38	–	–	–	–
	0.1	1.49/1.44	356	32.0	0.43	0.134	-0.005	0.047	0.092
	0.5	1.52/1.46	362	32.9	0.31	0.070	-0.021	0.031	0.060
	1.0	1.55/1.50	368	41.0	0.18	0.019	-0.038	0.019	0.038
Pyr1.6-TFSI	0.0	1.41/1.35	346	23.4	0.55	–	–	–	–
	1.0	1.48/1.43	344	34.8	0.34	0.013	-0.038	0.019	0.032

Table 2 Predicted properties: mass density ρ (at 300K for DMSO and at 300K/385K for Pyr1.X-TFSI), O_2 self diffusion coefficient D, viscosity ν (at 300K for DMSO and at 385K for Pyr1.X-TFSI), and ionic conductivity σ. Note the partial conductivities are defined by the per-species partial currents and hence a negative value indicates the species is flowing against the electrical bias due to co-transport with another species.

main essentially Maxwell-Boltzmann. (A distinctly bimodal distribution for DMSO would indicate a sub-population co-transporting with Li^+ by solvation with a significant average velocity and a quiescent excess population of the charge neutral DMSO that is not involved in solvation.) Only at higher biases E can we reliably extract the mean streaming velocity of the charged species $\mathbf{v}_a$, see Fig. 4, associated with the ionic currents.

We can infer some aspects of co-transport of solvating species from the inset of Fig. 4 and the coordination information in Fig. 5. The trend in the average velocity *vs.* bias is the same for all three electrolyte species. The trend for the neutral DMSO follows that of Li^+ albeit at a lower magnitude due to the excess DMSO, not needed for solvation, being quiescent/stagnant. Fig. 5a shows the coordination of Li^+ with other Li^+, the partially negatively charged O in DMSO, and the partially negatively charged O in $TFSI^-$. We see that Li^+ is strongly and prevalently solvated by the polar DMSO molecules, and this solvation is unaffected by the bias E over the range we studied, E=0.0–0.1 V/Å. The association of Li^+ by $TFSI^-$ is considerably weaker, as evidenced by the slope between the first ($R < 3$Å) and second ($R < 5$Å) shells, but intermingles with DMSO in the first shell, $R < 3$Å. (Here, the slope of the coordination graph is directly related to the presence of species between the dominant peaks of the RDF that define the first and second solvation shells.) Also, the weaker coordination of Li^+ with the charged $TFSI^-$ decreases with increased bias, as does the coordination with other Li^+. In the second shell, $R \in [3,8]$Å, all three species are present in significant quantities. Given the lack of a distinct plateau in the RDF profiles, we infer that this shell is "softer", *i.e.* less strongly bound and less well defined/more intermixed. This is supported by the presence of Li^+ in this shell and the persistence of $TFSI^-$ species in each of the shells shown in Fig. 5b. Here we see that the first shell is very stable, with one $TFSI^-$ leaving (and one entering) on average every 539 ps. It is interesting that this behavior does not change significantly with bias, and, hence, likely has thermal origins. This observation corroborates the assumption that the bias is not changing the solvation dynamics significantly. The second shell, on the other hand, is far less stable, with one $TFSI^-$ leaving the Li^+ coordination shell an order of magnitude faster (59 ps). (Note that, in Fig. 5b, the residency of species in the second shell is asymptoting to that of the first, as expected.)

3.2.2 LiTFSI/Pyr1.X-TFSI

Given the ionic nature and distinct structure of the Pyr-based ILs, we expect different transport and solvation mechanisms than in the DMSO electrolyte. For the ILs, we first examined how the range of ligand lengths affected the conformations of the solvent molecules. The RDFs in Fig. 6 show the predominant distances between the N in the Pyr ring and the C at the end of the exchangeable ligand in the Pyr ILs and gives an indication of cation radius in solution. All Pyr1.x display two peaks, where the first prominent peak occurs approximately at: 4.3Å for Pyr1.2O1, 3.9Å for Pyr1.3, 4.5Å for Pyr1.4, and 6.8Å for Pyr1.6. Interestingly, Pyr1.4 and Pyr1.6 have two primary peaks with the second peak at $\approx$ 5.1Å which implies these pyrrolidiniums have two comparably likely conformations in solution. Also, Pyr1.4 and Pyr1.6 are the only two of the four pyrrolidiniums studied which have a solvated length considerably shorter than their straight chain lengths (4.4Å for Pyr1.2O1, 3.9Å for Pyr1.3, 5.1Å for Pyr1.4, and 7.6Å for Pyr1.6). Although electrostatics and the particular solvation environment play a role, this suggests that these two pyrrolidiniums have flexible ligands and the shorter Pyr1.3 and the O containing Pyr1.2O1 have relatively stiff ligand chains.

Similar to DMSO, the E-field in the range 0–0.01 V/Å creates a negligible perturbation on the thermal distribution and there is no measurable sensitivity to molarity of Li^+ (not shown). As can be seen in Fig. 7 and Fig. 8, the Li^+ is primarily solvated by $TFSI^-$ and this coordination is effectively unchanged over the E biases and the types of Pyr ILs studied. The solvation shells are apparently stable in the external field. This is similar to the DMSO results; however, in this case the primary solvating species is $TFSI^-$. The second shell of $TFSI^-$ around Li^+ is marginally more pronounced in Pyr ILs than the second shell of DMSO. The weak Li^+:Li^+ association is somewhat sensitive to Li^+ molarity as the Li^+ crowd and intermix with Pyr1.4 and $TFSI^-$ the second

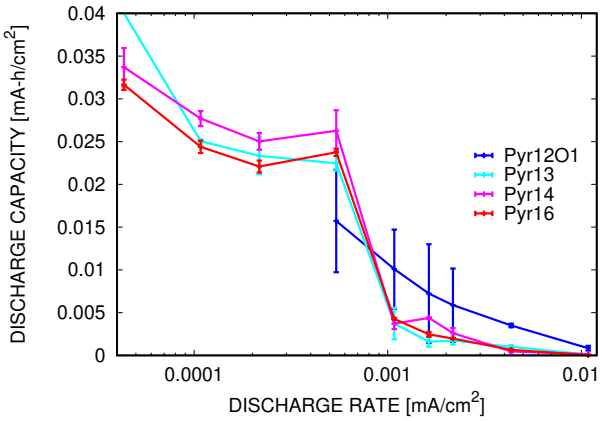

(a) Pyr1.X$^+$ structure

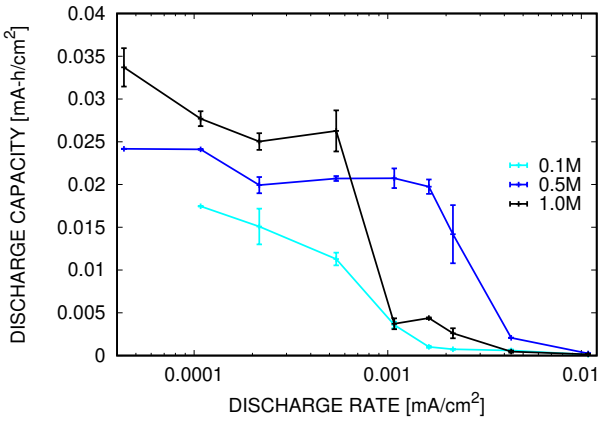

(b) LiTFSI concentration

Fig. 3 Discharge capacity as a function of discharge rate (a) 1.0M LiTFSI, and (b) Pyr1.4-TFSI. Discharge capacity and rate are normalized by the electrochemical active surface area (ECSA).

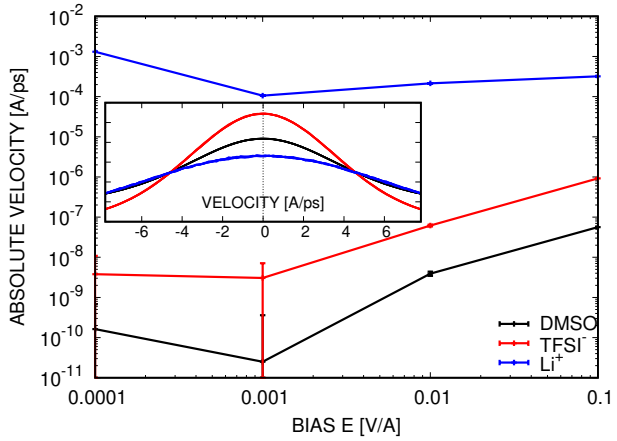

Fig. 4 1.0M LiTFSI/DMSO system: DMSO, TFSI$^-$ and Li$^+$ velocities over a range of bias E = 0.0001–0.1 V/Å, and (inset) velocity distributions for $E = \{0.0, 0.001, 0.01, 0.1\}$ V/Å.

shell of Li$^+$. Interestingly, the O in Pyr1.2O1 intermixes, in small amounts, in the second shell of TFSI$^-$ and, as is apparent from the DMSO results, this weaker interaction is marginally sensitive to E bias.

Unlike DMSO, the persistence analysis in Fig. 9 shows that both the first and second Li$^+$ solvation shells have a relatively high initial turnover rates compared to the inner shell of Li$^+$ in DMSO, implying that both the inner and outer shells are loosely bound; however, the asymptotic characteristics times, 36–61 ps and 255–397 ps, respectively, appear to imply that there is exchange between the two shells but the association with molecules at the limits of the outer shell is relatively stable with respect to exchange with bulk. Perhaps the TFSI$^-$ are less likely to find a stable arrangement near Li$^+$ due to the fact that they are larger than DMSO, but the electrostatic interactions also likely play a role. The use of the O atoms in TFSI$^-$ to track association with Li$^+$ likely also has an effect, in that any of the two pairs of negatively charged O atoms are equally probable to be in close association with the Li$^+$. Hence, they are likely to exchange with in the first shell, as we have defined it, but the TFSI$^-$ that the O atoms belong to will stay in more persistent association with the Li$^+$, as evidenced by the relative stability of the second shell. The propensity for the outer shell to be more stable than the inner is nearly identical across all the Pyr solvents with the lowest molarity solvent, 0.1M LiTFSI/Pyr1.4-TFSI, being somewhat of an outlier. Generally speaking, there is a small trend for the residence time (of a TFSI$^-$ near a Li$^+$) to increase with increasing Li$^+$ molarity; and, the longer alkyl chained Pyr ILs appear to enhance this residence time, with Pyr1.2O1-TFSI creating the most stable environment. Furthermore, the calculated characteristic TFSI$^-$:Li$^+$ residence times are correlated with the transport coefficients D (O_2 diffusivity) and σ (ionic conductivity). Despite no significant correlation ($\rho < 0.4$, where $0 \leq \rho \leq 1$ is the correlation coefficient) of D and σ with the residence time of first shell across Pyr1.X ILs at 1M, there is significant correlation of the relevant properties with the residence time of the second shell. The diffusion constant D of O_2 is anticorrelated, ρ = -0.84, with the residency time, and the ionic conductivity σ is directly correlated, $\rho = 0.96$. Across LiTFSI concentrations in Pyr1.4 the residence time of both shells and both properties are anticorrelated with $\rho <$ -0.95, and across all simulations the properties are anticorrelated with $\rho <$ -0.80. This implies that the characteristic residence time may be a good predictor of relative transport performance of ILs; however, there are lower, but significant correlations with viscosity (first shell: 0.49, second shell: 0.66) which may indicate these transport mechanisms are coordinated with viscosity effects. More data would improve confidence in these correlations.

The estimated ionic conductivity and molecular oxygen diffusivity for the various Pyr solvents is summarized in Table 2. In this table we report the partial/per-species ionic conductivities as well as the total. The total conductivities decrease with increasing Li$^+$ content and alkyl ligand length, with Pyr1.2O1-TFSI being an outlier with high conductivity which is correlated with solvation stability. Also, it is significant that the Li$^+$ partial conductivities are negative which indicates that Li$^+$ is co-transporting with TFSI$^-$. This phenomenon increases with increased Li$^+$ content and is essentially constant across Pyr ILs, with Pyr1.2O1-TFSI

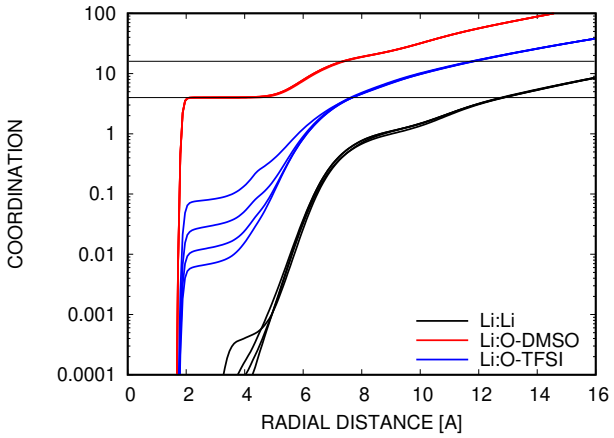

(a) Li^+ coordination

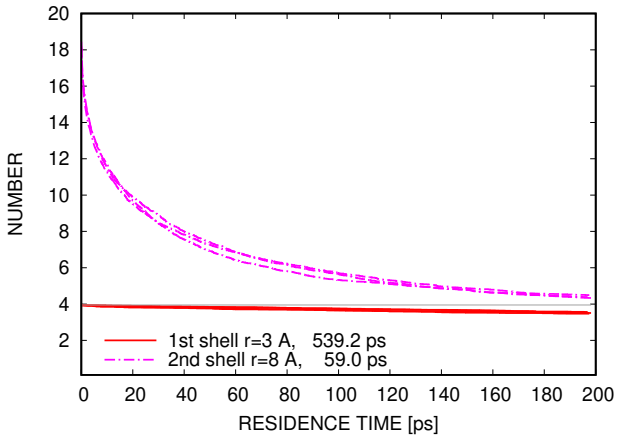

(b) residency of DMSO near Li^+

Fig. 5 1.0M LiTFSI/DMSO system: (a) Li^+ coordination over a range of bias $E = \{0.0, 0.001, 0.01, 0.1\}$ V/Å(gray horizontal lines mark levels for 4 and 16 coordinating DMSOs), and (b) residency time of DMSO in inner shell, inside 3.0 Å, and the inner and outer shells, inside 8.0 Å, of Li^+. The asymptotic residence time for the inner shell is 539.2 ps and for the outer shell 59.0 ps. Note coordination is the average number of molecules near a Li^+.

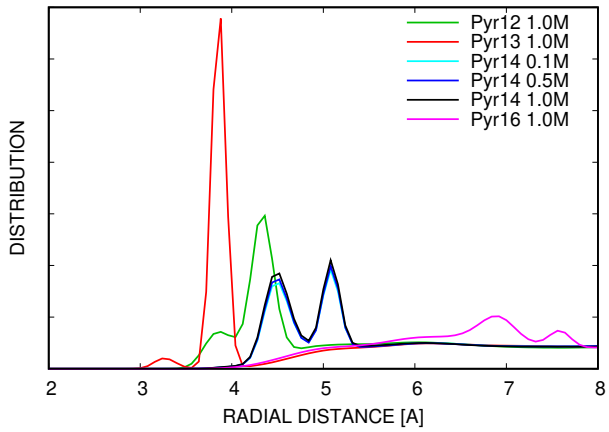

Fig. 6 Radial distribution of the distance from N in Pyr1.X^+ to the end C in the variable ligand (X).

again being an outlier with the least negative partial conductivity. More discussion of these findings will be given in the subsequent section.

With regard to the O_2 diffusion, molecular oxygen is small and non-polar so it is not particularly bound with any of the electrolyte species. The slightly elevated temperature needed to obtain the fluid model Pyr ILs will have the side-effect of inflating the O_2 diffusion estimates. Nevertheless, the O_2 appears to diffuse through the free space of a nearly solid/highly viscous solvent. We estimate mean cavity radius ≈ 0.8Å from the pre-diffusion/ballistic regime of mean squared displacement *vs.* time of O_2 diffusion. This result is slightly independent of Pyr^+ type, Pyr1.2O1$^+$: 0.78 Å, Pyr1.3$^+$: 0.79 Å, Pyr1.4$^+$: 0.78 Å, Pyr1.6$^+$: 0.82 Å, and effectively independent of Li^+ molarity. More discussion of these properties will be given in the next section in the context of the experimental results.

4 Discussion

From experiments we have measurements of several transport properties affecting cell performance, and from simulations we have corresponding estimates with molecular observations of solvation. Fig. 10 compares the measured ionic conductivity and O_2 diffusion coefficient in Table 1 with the computed properties reported in Table 2. Both experiment and simulation agree that increased Pyr1.X^+ alkyl chain length inhibits ion conduction. Pyr1.2O1$^+$ is notably off-trend, acting like a smaller alkyl chain Pyr^+ electrolyte than its size suggests. Since uncoordinated Pyr1.2O1$^+$ has a higher diffusivity than the same species in a Li^+ coordinated environment and can still carry charge, the total electrolyte conductivity may be greater, as we see in our experimental results, and yet the partial Li^+ conductivity, the key metric of importance, is worse. Disregarding the 0.0M Li^+ electrolytes, our experiments and simulations suggest that ionic conductivity also decreases with increasing Li^+ concentration. The effect on the total conductivity can in part be attributed to increases in electrolyte viscosity, but also to structural changes involving Li^+ coordination[46]. Fig. 2 shows that the experimental measurements of ionic conductivity have the same general trend with Li^+ concentration across different Pyr ILs. (The slight increase in conductivity of Pyr1.4$^+$ with Li salt concentration is statistically insignificant.) To more thoroughly understand the influences of solution structure on ionic conductivity, it is useful to compare results from IL systems to those from a standard DMSO electrolyte.

4.1 Ionic Conduction

From experimental data in Table 1 and simulation data in Table 2, we find that lithium mobility is lower in ILs than in an aprotic DMSO solvent. In DMSO based electrolytes, ionic conductivity increases with Li^+ content unlike in Pyr IL electrolytes. As our simulations reveal, there are qualitative differences in how Li^+ is solvated in the two classes of electrolytes. The model shows that in DMSO, Li^+ is primarily coordinated with polar, charge neutral DMSO and to a much lesser degree with $TFSI^-$ ions. In Pyr ILs, the dominant Li^+ coordination is by $TFSI^-$ while the Pyr^+

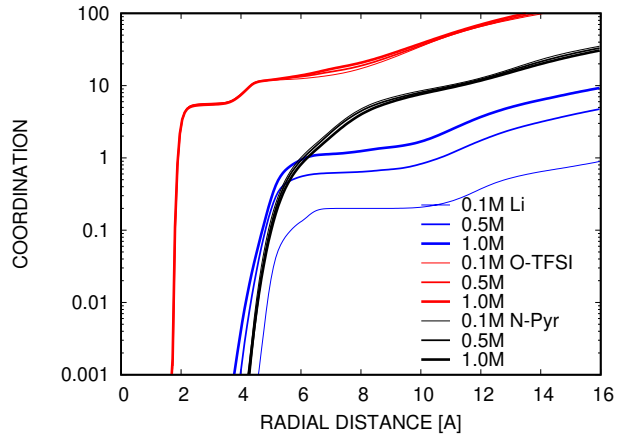

(a) LiTFSI molarity

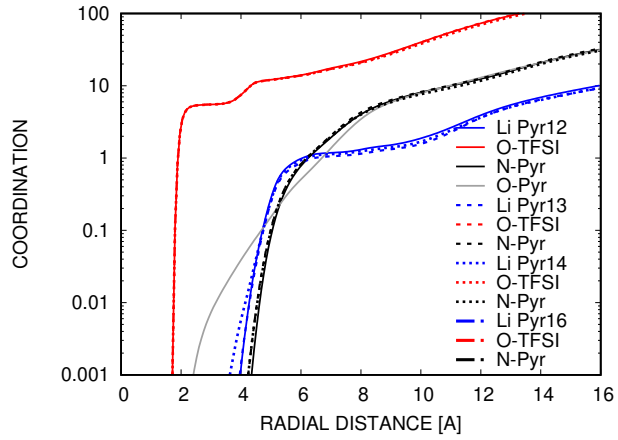

(b) Pyr1.X$^+$ structure

Fig. 7 Radial distribution of Li^+ coordination with solvent species, dependence on (a) LiTFSI molarity in LiTFSI/Pyr1.4-TFSI and on (b) Pyr1.X$^+$ structure with 1.0M LiTFSI. Li Pyr12 denotes the Li^+:Li^+ coordination in Pyr1.2O1, O-TFSI denotes the Li^+:TFSI coordination were O-TFSI is the O in $TFSI^-$, N-Pyr denotes the N in Pyr1.X$^+$, *etc.*

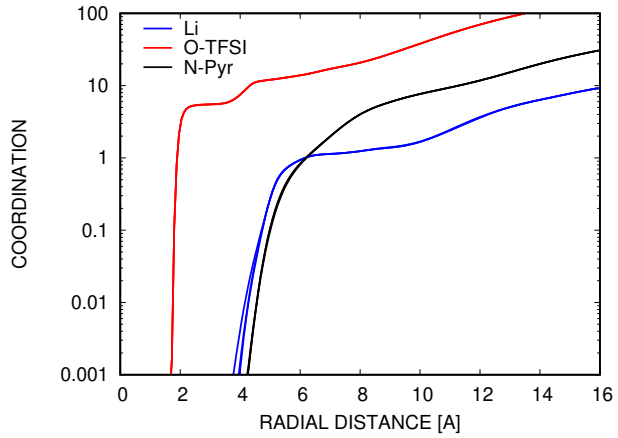

(a) 1.0M LiTFSI/Pyr1.4-TFSI

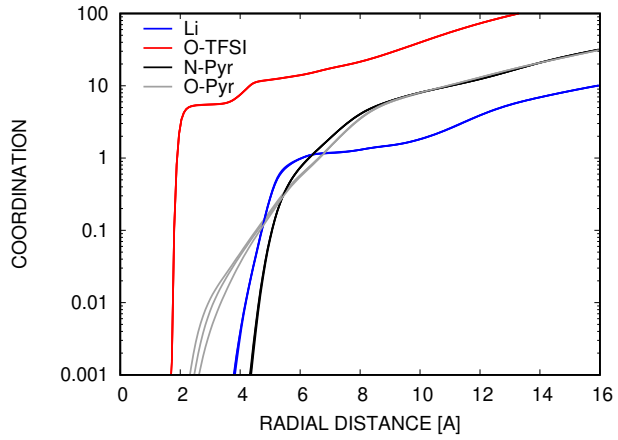

(b) 1.0M LiTFSI/Pyr1.2O1-TFSI

Fig. 8 Shift with electrical bias (E=0.001–0.1 V/Å) of Li^+ coordination with electrolyte species. O-TFSI denotes the O in $TFSI^-$, N-Pyr denotes the N in Pyr1.X$^+$, *etc.*

species only appear in the second shell. In DMSO, Li^+ has a stable inner shell coordination (and an erodible outer shell), while in Pyr ILs, the Li^+ coordination with $TFSI^-$ has low persistence as Fig. 5 and Fig. 9 demonstrate. This suggests that the Li^+ transport in the two types of electrolytes could be primarily by different mechanisms, *e.g.* "vehicular" diffusion of a persistent solvation structure *vs.* "structural" diffusion [19,20]. Similar to Haskins *et al.*[22] and Castiglione *et al.*[19,20], we observe an influence of Li^+ concentration on this mechanism. Fig. 9 shows marginally increased residence time with increasing Li^+ concentration, correlated with a decrease in ionic conductivity. No significant changes to the solvation structure are necessary, as Fig. 7 indicates; however, the turnover rate of the particular molecules in the solvation shells is important, as our correlation results in Sec. 3.2.2 demonstrate. It is plausible that in Pyr IL electrolytes, Li^+ mobility and conductivity decrease with higher concentrations of LiTFSI due to increased dielectric screening by the $TFSI^-$ anions, or due to a decrease in the amount of free, uncoordinated species that are necessary for structural diffusion (since more than one $TFSI^-$ is needed to fully solvate Li^+). There are a few reports that note an increase in Li^+ mobility with increasing concentration over limited concentration ranges [46], but these are typically in situations where Li^+ cations are highly dissociated and sparse or anions are immobilized and thus result in high Li^+ transference numbers (*i.e.* ionic plastic crystals) [56,57]. For traditional ionic liquid electrolytes at room temperature like those we studied, the inverse Li^+ mobility-concentration relationship generally holds.

The quantitative difference in the experimental and simulated trends of the ionic conductivity with LiTFSI molarity, shown in Fig. 10, is likely due to the relatively small increase in viscosity with increasing salt content predicted by the molecular model. One benefit of this minimal change in viscosity in the molecular model is that it isolates other effects influencing ionic conductivity.

Although of limited accuracy in the case of relatively small molecular oxygen or charged Li^+ ions migrating in Pyr1.X solvents, the often cited Stokes-Einstein relationship suggests the diffusion coefficient D for either is inversely proportional to the viscosity η of the solvent and the effective (solvated) radius of the particular solute. So for O_2 we expect its diffusivity to be hin-

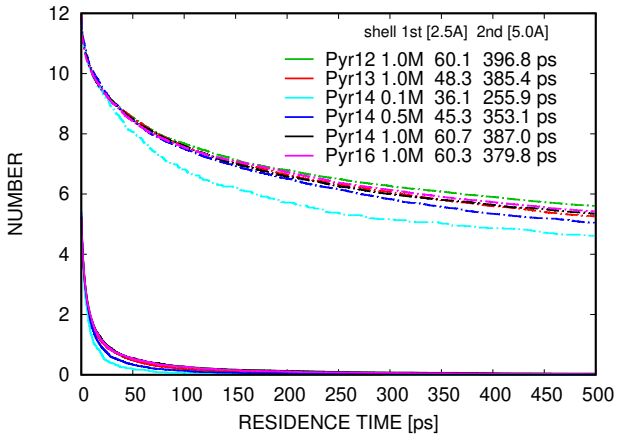

Fig. 9 LiTFSI/Pyr1.X-TFSI: $TFSI^-$ residence time in the inner, within 2.5 Å, and outer, 5.0 Å, shells of Li^+. Times given in the legend are asymptotic characteristic times extracted from exponential fits to the data.

dered by the viscosity of the ILs. Since the Einstein-Smoluchowski relationship provides a direct correlation of D with mobility μ, the mobility of Li^+ and the ionic conductivity (at fixed salt concentration) should be inversely proportional to the viscosity and effective radius. Given the lack of stability of the Li^+ coordination shells in Pyr ILs, the effective $\bar{R}$ is likely smaller than even the radius of the first shell and comparable to that of the tighter Li^+ coordination shell in DMSO. So, if Stokes-Einstein is modified to reflect a soft solvation shell radius, we would expect that the Li+ partial conductivity in Pyr ILs to be 1/100 that of DMSO. The actual Li^+ partial conductivity is only 1/10 that of DMSO, but if we account for reasonable estimates of Li^+ transference number (*e.g.* 0.1 for Pyr ILs and 0.5 for DMSO), the agreement is much better. This gives credence to a greater degree of "structural" diffusion in Pyr ILs where the exchange of species in the Li^+ coordination sphere occurs.

We note that a key difference between the experimental measurements and the simulations of ionic conductivity is derived from the model configuration. In a real cell, only Li^+ can sustain steady-state transport since it is liberated and incorporated at the electrodes while the other electrolyte species are blocked by the electrodes. In contrast, in our simulations all species, and in particular $TFSI^-$, can flow freely. Since the Li^+ appear to be tightly coordinated with multiple $TFSI^-$ they tend to transport against the electrical bias which results in negative partial ionic conductivities. Interestingly Gouverneur *et al.*[58] also reports negative effective Li^+ transference numbers (and partial conductivities) in LiTFSI/EMIM-TFSI systems due to Li^+ co-transport with anions, but these electrophoretic NMR experiments, like our simulations, have short time scales that do not allow the buildup of concentration gradients. If the $TFSI^-$ were on average stagnant, as in a cell, the effective partial conductivities of Li^+ would increase, as would the total ionic conductivities which are already on par with the measured ones. This difference also likely affects the proportion of Li^+ "structural" diffusion *vs.* persistent-solvation diffusion we observe in our model. For this reason, we cannot definitively say that a particular transport mechanism dominates. From prior literature, we know that the Li^+ transference number in IL electrolytes (not including ionic plastic crystals) is generally in the range 0.04–0.07[59] to 0.06–0.13[47]. Li^+ ions, thus, do not contribute very significantly to the overall conductivity of the electrolyte. Since Li^+ is the functional component in Li-ion and Li-air cells, this is quite discouraging for the ability of Li^+-containing ionic liquid electrolytes to demonstrate high power capability. Yet, even a small improvement in electrolyte design that enhances Li^+ mobility (*e.g.* by reducing solvation persistence) is likely to have a significant impact on device performance.

4.2 Oxygen Transport

The oxygen diffusivity results in Fig. 10 illustrate distinct trends with $Pyr1.X^+$ alkyl chain length and Li^+ concentration. Molecular oxygen diffusivity D correlates positively with alkyl ligand length but negatively with Li^+ concentration. Given the computed and experimentally measured densities of our Pyr IL systems, it appears that the longer alkyl chains do not pack as efficiently, leaving intermolecular spaces through which O_2 diffuse. However, our simulations imply that the diffusion mean free paths of O_2 (and mean cavity radius in the solution) only change marginally with different Pyr cations. Small, non-polar O_2 molecules diffuse in an essentially classical manner (*i.e.* a quadratic pre-diffusion/ballistic regime followed by a perfectly linear mean squared displacement). This behavior was observed in our model at the elevated temperature needed to prevent the ILs becoming glassy. This necessary adjustment had the predictable side-effect of increasing the D estimates above the experimental values due to the lower viscosities of the ILs and the increased kinetic energy of the molecular oxygen, refer to Fig. 10b. Below this temperature, the mean squared displacement and the molecular trajectories were largely diffusive but did exhibit evidence of O_2 being trapped in void spaces in the solution. Since there are indications that run contrary to the simple free volume perspective, we conjecture that the mechanisms dominating O_2 diffusion and solubility are more dynamic and likely influenced by the fact that the ILs are near their melt temperatures. In addition, the negative trend of O_2 diffusivity D with increasing Li^+ concentration in the simulations is most likely due to the increase in viscosity if we assume the Stokes-Einstein model is applicable for molecular oxygen. For example, the fact that the diffusion coefficient D for O_2 is correlated with the residence time of $TFSI^-$, the primary Li^+ solvating species, indicates that the transport of the species are connected (a mechanism that simple free volume theories of molecular diffusion ignore).

4.3 Device Impact

In the guiding context of limiting current, Eq. (1), where $i_{\lim} \sim Dc/\nu$, it appears that Li^+, not O_2, is the limiting component in Pyr IL electrolytes given its relatively poor transport properties. In Pyr ILs, the O_2 diffusion coefficient D and viscosity ν are inversely-correlated with Li^+ concentration as Fig. 2, Fig. 10a, Table 1, and Table 2 indicate. Hence, an optimum electrolyte composition dependent on Pyr cation and Li^+ concentration exists. We reason, based on experimental and simulated transport properties, that

Pyr ILs with intermediate Li^+ concentrations (of ≈0.5M) and smaller Pyr cations with pure alkyl ligands will outperform similar compositions with respect to rate capability/power. Nevertheless, off-trend improvements by Pyr cations with variations on pure alkyl ligands are possible, as our Pyr1.2O1$^+$ results shows.

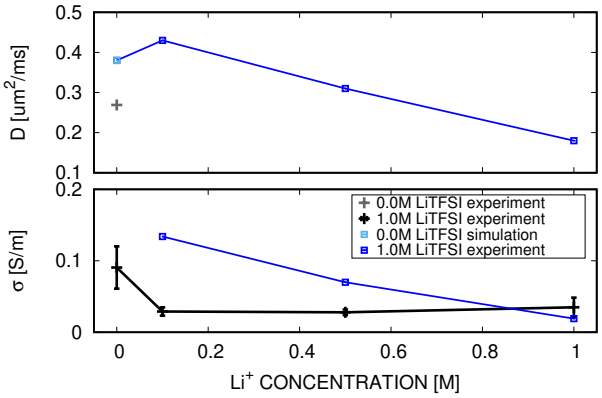

(a) Pyr1.4-TFSI

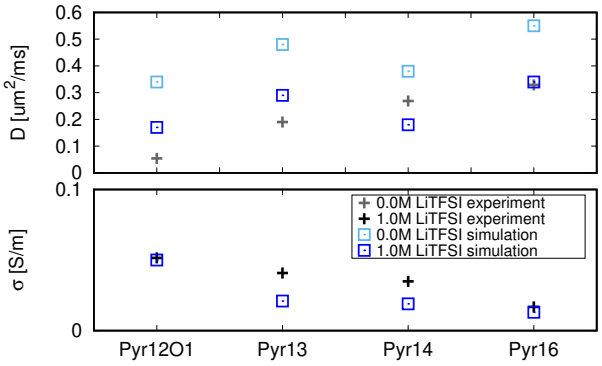

(b) Pyr1.X-TFSI

Fig. 10 Comparison of ionic conductivity σ and O_2 diffusion coefficient D. Note that experimental O_2 diffusion measurements were obtained from ILs without LiTFSI.

5 Conclusion

In this work we employed experiments and molecular simulations to explore the influence of Pyr IL structure and electrolyte composition on transport behaviors in Li-air and Li-ion relevant environments. We show that:

- In LiTFSI/Pyr1.X-TFSI electrolytes, Pyr1.X$^+$ cation structure can influence electrolyte conductivity even without intimate interactions with Li^+. This is caused by subtle differences in the persistence of $TFSI^-$ species within the first and second Li^+ solvation shells, as well as electrolyte viscosity.
- Increasing the Li^+ concentration in Pyr1.X-TFSI electrolytes generally decreases the electrolyte conductivity. This is, in part, explained by increasing persistence of the Li^+ solvation sphere which makes "structural" diffusion of Li^+ more challenging.
- The diffusivity of O_2 is improved by lengthening the alkyl ligand on a Pyr1.X$^+$ cation. Since O_2 is a non-polar, non-coordinating species, its transport is likely aided by more weakly-coordinating/looser alkyl environments.
- Intermediate Li^+ concentrations (≈0.5 M LiTFSI) appear to optimize the rate limiting behavior of Li-air cells by balancing Li^+ mobility with Li^+ concentration. By analyzing several Pyr1.X-TFSI systems, we find that Li^+ is the most likely limiting reactant in Li-air cells of this type.

By uniting electrochemical experiments and molecular simulations, we have achieved a better understanding of the complex and subtle impact of ionic liquid structure on electrolyte dynamics. These findings demonstrate that systematic design of ionic liquid electrolytes to optimize device performance is not only possible, but highly desirable.

Conflicts of interest

There are no conflicts to declare.

Acknowledgements

Sandia National Laboratories is a multimission laboratory managed and operated by National Technology and Engineering Solutions of Sandia, LLC., a wholly owned subsidiary of Honeywell International, Inc., for the U.S. Department of Energy's National Nuclear Security Administration under contract DE-NA-0003525. The views expressed in the article do not necessarily represent the views of the U.S. Department of Energy or the United States Government.

Notes and references

1 F. S. Gittleson, R. E. Jones, D. K. Ward and M. E. Foster, *Energy & Environmental Science*, 2017, **10**, 1167–1179.
2 D. Sharon, M. Afri, M. Noked, A. Garsuch, A. A. Frimer and D. Aurbach, *The Journal of Physical Chemistry Letters*, 2013, **4**, 3115–3119.
3 D. G. Kwabi, T. P. Batcho, C. V. Amanchukwu, N. Ortiz-Vitoriano, P. Hammond, C. V. Thompson and Y. Shao-Horn, *The Journal of Physical Chemistry Letters*, 2014, **5**, 2850–2856.
4 N. Mozhzhukhina, L. P. Méndez De Leo and E. J. Calvo, *The Journal of Physical Chemistry C*, 2013, **117**, 18375–18380.
5 K. U. Schwenke, S. Meini, X. Wu, H. A. Gasteiger and M. Piana, *Physical Chemistry Chemical Physics*, 2013, **15**, 11830–11839.
6 K. R. Ryan, L. Trahey, B. J. Ingram and A. K. Burrell, *The Journal of Physical Chemistry C*, 2012, **116**, 19724–19728.
7 G. Elia, J. Hassoun, W.-J. Kwak, Y.-K. Sun, B. Scrosati, F. Mueller, D. Bresser, S. Passerini, P. Oberhumer, N. Tsiouvaras *et al.*, *Nano letters*, 2014, **14**, 6572–6577.
8 G. A. Elia, U. Ulissi, S. Jeong, S. Passerini and J. Hassoun, *Energy & Environmental Science*, 2016, **9**, 3210–3220.
9 G. Appetecchi, M. Montanino and S. Passerini, *ACS Symposium Series: Ionic Liquids Science and Applications*, 2013, **1117**, 67–128.

10 S. Monaco, F. Soavi and M. Mastragostino, *The journal of Physical Chemistry Letters*, 2013, **4**, 1379–1382.

11 S. Das, J. Højberg, K. B. Knudsen, R. Younesi, P. Johansson, P. Norby and T. Vegge, *The Journal of Physical Chemistry C*, 2015, **119**, 18084–18090.

12 M. L. P. Le, F. Alloin, P. Strobel, J.-C. Leprêtre, C. Pérez del Valle and P. Judeinstein, *The Journal of Physical Chemistry B*, 2009, **114**, 894–903.

13 A. Martinelli, A. Matic, P. Jacobsson, L. Borjesson, A. Fernicola and B. Scrosati, *The Journal of Physical Chemistry B*, 2009, **113**, 11247–11251.

14 S. Tsuzuki, W. Shinoda, H. Saito, M. Mikami, H. Tokuda and M. Watanabe, *The Journal of Physical Chemistry B*, 2009, **113**, 10641–10649.

15 Z. J. Chen, T. Xue and J.-M. Lee, *RSC Advances*, 2012, **2**, 10564–10574.

16 S. Tang, G. A. Baker and H. Zhao, *Chemical Society Reviews*, 2012, **41**, 4030–4066.

17 G. A. Giffin, J. Tannert, S. Jeong, W. Uhl and S. Passerini, *The Journal of Physical Chemistry C*, 2015, **119**, 5878–5887.

18 M. Kar, B. Winther-Jensen, M. Armand, T. J. Simons, O. Winther-Jensen, M. Forsyth and D. R. MacFarlane, *Electrochimica Acta*, 2016, **188**, 461–471.

19 F. Castiglione, E. Ragg, A. Mele, G. B. Appetecchi, M. Montanino and S. Passerini, *The Journal of Physical Chemistry Letters*, 2011, **2**, 153–157.

20 F. Castiglione, A. Famulari, G. Raos, S. V. Meille, A. Mele, G. B. Appetecchi and S. Passerini, *The Journal of Physical Chemistry B*, 2014, **118**, 13679–13688.

21 V. Lesch, S. Jeremias, A. Moretti, S. Passerini, A. Heuer and O. Borodin, *The Journal of Physical Chemistry B*, 2014, **118**, 7367–7375.

22 J. B. Haskins, W. R. Bennett, J. J. Wu, D. M. Hernández, O. Borodin, J. D. Monk, C. W. Bauschlicher Jr and J. W. Lawson, *The Journal of Physical Chemistry B*, 2014, **118**, 11295–11309.

23 A. J. Bard and L. R. Faulkner, *Electrochemical methods: fundamentals and applications*, Wiley, New York, 2nd edn, 2001.

24 J. Read, K. Mutolo, M. Ervin, W. Behl, J. Wolfenstine, A. Driedger and D. Foster, *Journal of The Electrochemical Society*, 2003, **150**, A1351–A1356.

25 A. Schürmann, R. Haas, M. Murat, N. Kuritz, M. Balaish, Y. Ein-Eli, J. Janek, A. Natan and D. Schröder, *Journal of The Electrochemical Society*, 2018, **165**, A3095–A3099.

26 A. K. Burrell, R. E. Del Sesto, S. N. Baker, T. M. McCleskey and G. A. Baker, *Green Chemistry*, 2007, **9**, 449–454.

27 G. B. Appetecchi, M. Montanino, D. Zane, M. Carewska, F. Alessandrini and S. Passerini, *Electrochimica Acta*, 2009, **54**, 1325–1332.

28 D. Shoup and A. Szabo, *Journal of Electroanalytical Chemistry and Interfacial Electrochemistry*, 1982, **140**, 237–245.

29 A. R. Neale, P. Li, J. Jacquemin, P. Goodrich, S. C. Ball, R. G. Compton and C. Hardacre, *Physical Chemistry Chemical Physics*, 2016, **18**, 11251–11262.

30 D. McFarlane, J. Sun, J. Golding, P. Meakin and M. Forsyth, *Electrochimica Acta*, 2000, **45**, 1271–1278.

31 W. D. Cornell, P. Cieplak, C. I. Bayly, I. R. Gould, K. M. Merz, D. M. Ferguson, D. C. Spellmeyer, T. Fox, J. W. Caldwell and P. A. Kollman, *Journal of the American Chemical Society*, 1995, **117**, 5179–5197.

32 W. L. Jorgensen, D. S. Maxwell and J. Tirado-Rives, *J. Am. Chem. Soc*, 1996, **118**, 11225–11236.

33 J. Wang, R. M. Wolf, J. W. Caldwell, P. A. Kollman and D. A. Case, *Journal of Computational Chemistry*, 2004, **25**, 1157–1174.

34 R. W. Hockney and J. W. Eastwood, *Computer simulation using particles*, CRC Press, 1988.

35 S. J. Weiner, P. A. Kollman, D. T. Nguyen and D. A. Case, *Journal of Computational Chemistry*, 1986, **7**, 230–252.

36 T. Fox and P. A. Kollman, *The Journal of Physical Chemistry B*, 1998, **102**, 8070–8079.

37 J.-C. Soetens, C. Millot and B. Maigret, *The Journal of Physical Chemistry A*, 1998, **102**, 1055–1061.

38 C. F. Lopez, S. O. Nielsen, M. L. Klein and P. B. Moore, *The Journal of Physical Chemistry B*, 2004, **108**, 6603–6610.

39 W. Jiang, Y. Wang and G. A. Voth, *The Journal of Physical Chemistry B*, 2007, **111**, 4812–4818.

40 M. J. Frisch, *Gaussian*, Gaussian Inc. Wallingford CT, http://gaussian.com, 2016.

41 C. M. Breneman and K. B. Wiberg, *Journal of Computational Chemistry*, 1990, **11**, 361–373.

42 S. Plimpton, *LAMMPS : Large-scale Atom/Molecular Massively Parallel Simulator*, Sandia National Laboratories, http://lammps.sandia.gov, 2018.

43 R. Jones, D. Ward, F. Gittleson and M. Foster, *Journal of The Electrochemical Society*, 2017, **164**, A1258–A1267.

44 D. Ward, R. Jones, J. Templeton, K. Reyes and M. Kane, *ECS Transactions*, 2014, **61**, 181–191.

45 G. Ciccotti and G. Jacucci, *Physical Review Letters*, 1975, **35**, 789.

46 H. Yoon, A. S. Best, M. Forsyth, D. R. MacFarlane and P. C. Howlett, *Physical Chemistry Chemical Physics*, 2015, **17**, 4656–4663.

47 T. Frömling, M. Kunze, M. Schönhoff, J. Sundermeyer and B. Roling, *The Journal of Physical Chemistry B*, 2008, **112**, 12985–12990.

48 S. Monaco, A. M. Arangio, F. Soavi, M. Mastragostino, E. Paillard and S. Passerini, *Electrochimica Acta*, 2012, **83**, 94–104.

49 H. Weingärtner, *Angewandte Chemie International Edition*, 2008, **47**, 654–670.

50 K. Fruchey, C. M. Lawler and M. Fayer, *The Journal of Physical Chemistry B*, 2012, **116**, 3054–3064.

51 Y. Zhang and C. Pozo-Gonzalo, *Chemical Communications*, 2018, **54**, 3800–3810.

52 J. Bockris and H. Egan, *Transactions of the Faraday Society*, 1948, **44**, 151–159.

53 B. D. Adams, C. Radtke, R. Black, M. L. Trudeau, K. Zaghib and L. F. Nazar, *Energy & Environmental Science*, 2013, **6**,

1772–1778.

54 Y. Liu, L. Suo, H. Lin, W. Yang, Y. Fang, X. Liu, D. Wang, Y.-S. Hu, W. Han and L. Chen, *Journal of Materials Chemistry A*, 2014, **2**, 9020–9024.

55 R. Battino, *Oxygen and ozone. IUPAC solubility data series. Vol. 7*, 1981.

56 D. R. MacFarlane, J. Huang and M. Forsyth, *Nature*, 1999, **402**, 792.

57 Y. Zhou, X. Wang, H. Zhu, M. Armand, M. Forsyth, G. W. Greene, J. M. Pringle and P. C. Howlett, *Physical Chemistry Chemical Physics*, 2017, **19**, 2225–2234.

58 M. Gouverneur, F. Schmidt and M. Schönhoff, *Physical Chemistry Chemical Physics*, 2018, **20**, 7470–7478.

59 F. Wohde, M. Balabajew and B. Roling, *Journal of The Electrochemical Society*, 2016, **163**, A714–A721.

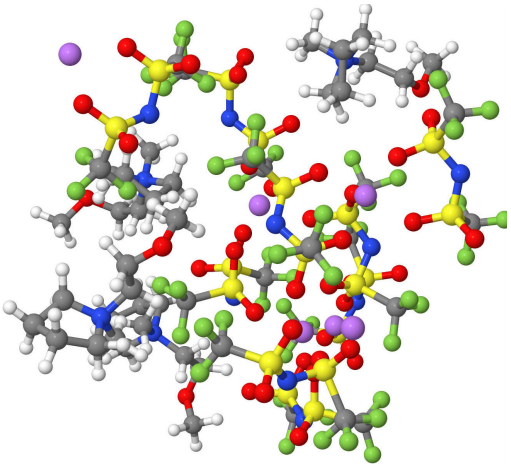

Using experiments and molecular simulations, we evaluate pyrrolidinium-based ionic liquid Li electrolytes and find that Li^+ and O_2 transport can be enhanced by varying the pyrrolidinium structure and Li concentration.